

PMP-Swin: Multi-Scale Patch Message Passing Swin Transformer for Retinal Disease Classification

Zhihan Yang, Zhiming Cheng, Tengjin Weng, Shucheng He, Yaqi Wang, Xin Ye, Shuai Wang

Abstract—Retinal disease is one of the primary causes of visual impairment, and early diagnosis is essential for preventing further deterioration. Nowadays, many works have explored Transformers for diagnosing diseases due to their strong visual representation capabilities. However, retinal diseases exhibit milder forms and often present with overlapping signs, which pose great difficulties for accurate multi-class classification. Therefore, we propose a new framework named Multi-Scale Patch Message Passing Swin Transformer for multi-class retinal disease classification. Specifically, we design a Patch Message Passing (PMP) module based on the Message Passing mechanism to establish global interaction for pathological semantic features and to exploit the subtle differences further between different diseases. Moreover, considering the various scale of pathological features we integrate multiple PMP modules for different patch sizes. For evaluation, we have constructed a new dataset, named OPTOS dataset, consisting of 1,033 high-resolution fundus images photographed by Optos camera and conducted comprehensive experiments to validate the efficacy of our proposed method. And the results on both the public dataset and our dataset demonstrate that our method achieves remarkable performance compared to state-of-the-art methods.

Index Terms—Deep learning, transformer, patch message passing, fundus image, multi-class disease classification,

I. INTRODUCTION

Retinal diseases, such as diabetic retinopathy (DR), age-related macular degeneration (AMD), and retinopathy of prematurity (ROP), are some of the leading causes of blindness worldwide [1]. Regular retinal examinations can facilitate early disease diagnosis before the manifestation of any symptomatic indications. Timely identification is of paramount significance

This work was supported in part by the Zhejiang Provincial Natural Science Foundation of China under Grant LDT23F01015F01, in part by the National Natural Science Foundation of China under Grant 62201323, and in part by the Natural Science Foundation of Jiangsu Province under Grant BK20220266. (First author: Zhihan Yang.) (Corresponding authors: Yaqi Wang; Xin Ye; Shuai Wang.)

Zhihan Yang is with School of Mechanical, Electrical and Information Engineering, Shandong University, Weihai, China (e-mail: yangzhihan@mail.sdu.edu.cn).

Zhiming Cheng is with School of Automation, Hangzhou Dianzi University, Hangzhou, China (email: czming@hdu.edu.cn).

Tengjin Weng is with School of Computer Science and Technology, Zhejiang Sci-Tech University, Hangzhou, China (email: wtjdsb@gmail.com).

Yaqi Wang is with the College of Media Engineering, Communication University of Zhejiang, Hangzhou, China (e-mail: wangyaqi@cuz.edu.cn).

Shucheng He and Xin Ye are with the Center for Rehabilitation Medicine, Department of Ophthalmology, Zhejiang Provincial People's Hospital (Affiliated People's Hospital, Hangzhou Medical College), Hangzhou, China (email: hscflea@163.com; yexinsarah@163.com).

Shuai Wang is with School of Cyberspace, Hangzhou Dianzi University, Hangzhou, China, and Suzhou Research Institute of Shandong University, Suzhou, China (e-mail: shuaiwang.tai@gmail.com).

as it can prevent complete vision loss in patients and potentially impede or halt degenerative conditions through prompt treatment regimens [2].

Diagnosing retinal disease often requires comprehensive consideration by clinically experienced ophthalmologists and specialists, a process that is not only very time-consuming and labor-intensive. In populous countries like India, the scarcity of well-trained ophthalmologists poses a significant challenge in addressing the pressing need for comprehensive eye care [3]. Consequently, there has been a growing reliance on automated analysis and diagnostic systems, such as artificial intelligence-based AI medical screening systems [4]–[6], which not only help alleviate the burden on healthcare personnel but also provide comparable diagnostic outcomes [7]. Particularly, deep learning-based methods for retinal disease diagnosis have been actively investigated.

Early deep learning-based approaches for diagnosis typically use Convolutional Neural Networks (CNNs) as CNNs have a strong ability to extract features of images. For instance, Asif et al. [8] propose a deep residual network based on the popular CNN architecture ResNet50 for the classification of multiple retinal diseases including DME, choroidal neovascularization (CNV), and DRUSEN. Y.T. et al. [9] propose an end-to-end two-branch network based on the EfficientNet, which can automatically classify various retinal diseases and solve problems with severe class imbalance. Pan et al. [10] design an automated deep learning-based system using Inceptionv3 and ResNet50 for categorizing fundus images into three classes, namely normal, macular degeneration, and tessellated fundus for timely recognition and treatment.

However, CNNs focus on local features and cannot establish long-range connectivity of images. This contradicts the need to focus on the relationship between local lesions and the overall retina in the classification of retinal diseases. Therefore, very recently, another popular deep learning architecture called Vision Transformer (ViT) [11] has been applied for retinal disease diagnosis because its self-attention mechanism can capture long-range associations effectively. For instance, Yu et al. [12] explore the applicability of ViT for retinal disease classification tasks and integrate Multiple Instance Learning into ViT to fully exploit the feature representations in fundus images. Junyong Shen et al. [13] propose a Structure-Oriented ViT (SoT) for retinal disease grading, which can further construct the relationship between lesions and the whole retina.

Although the based approach focuses on capturing global features, overcoming the weakness of CNNs, it ignores local features to some extent. For some diseases, the lesion area is fixed in the retina, for example, macular degeneration usually

occurs in the central region of the retina [14]. Ignoring such local information may lead to a decrease in disease detection performance. Solving this problem requires the model to balance the ability to capture long-range and local relationships.

Another issue is that, in contrast to the classification of natural objects, accurate multi-class classification of retinal diseases is challenging due to the presence of mild forms and overlapping signs. Conditions such as hard exudate, sub-retinal hemorrhage, neovascularization, pigment epithelial detachment, and macular atrophy can be observed in various retinal diseases including wet age-related macular degeneration (AMD), polypoidal choroidal vasculopathy (PCV), choroidal neovascularization, macular atrophy, retinal angiomatous proliferation, and idiopathic macular telangiectasia [15]. Thus, it is essential to fully explore the subtle differences between diseases, which requires the model to extract more complex feature representations from retinal images.

In addition, the various sizes of pathological features in fundus images across different diseases is a crucial aspect that has been overlooked in existing related works since certain diseases may only affect a small part of the retina, while others may spread across the entire retina. Thus, the approach aimed at recognizing different diseases should possess the ability to identify and distinguish various scales of lesions.

In this work, we propose a novel framework named Multi-Scale Patch Message Passing Swin Transformer (PMP-Swin) to address the mentioned challenges. Specifically, we adopt the pre-trained Swin Transformer as the backbone because its special pyramid architecture and shift window-based self-attention enable it to capture both global and local features effectively. Inspired by the fact that lesions of retinal diseases are usually scattered throughout various locations in the fundus image or concentrated in a large area, we design a Patch Message Passing (PMP) module to achieve fine-grained semantic understanding by constructing semantic interactions between each patch of the feature map. Finally, considering the various scales of disease regions, we integrate multiple PMP modules to construct interactions for different patch sizes. We conduct comprehensive experiments on both our private and public datasets to verify the proposed method's effectiveness. Our key contributions can be summarized as follows:

- 1) We design a novel PMP module based on the message-passing mechanism to construct semantic associations between patches output by Swin Transformer. The PMP module can effectively help discriminate confusing lesion features, achieving a more accurate diagnosis.

- 2) To recognize lesions with various scales better, multi-scale PMP modules for different-sized patches are attached to the Swin Transformer.

- 3) We build a new OPTOS dataset, with 1033 high-resolution colorful fundus images, and show through experiments that our proposed framework PMP-Swin can achieve higher accuracy than previous methods.

II. RELATED WORK

A. CNN based Methods

Extensive methods with CNN architecture have been proposed for retinal disease classification because of the automatic

feature extraction ability of CNN networks, which eliminates the need for manual intervention [16]–[18]. Most of the existing works are based on optimizing the classic CNN architectures, such as ResNet proposed by He et al. [19], XceptionNet proposed by Chollet [20], for the specific problem of retinal disease diagnosis, thus achieving more accurate diagnosis. For example, Sengar et al. [21] propose a novel deep learning-based multi-layer neural network architecture EyeDeep-Net for the classification of fundus images and non-invasive diagnosis of various eye diseases. Unfortunately, methods based on CNN architectures cannot fully solve the limitation of CNN itself, which is to focus on local attention, and thus cannot effectively extract global semantic information, making precise diagnosis remain challenging. Yang et al. [22] propose a feature extraction network DSRA-CNN based on the Xception architecture to achieve the classification of eight different fundus diseases on the ODIR dataset.

Therefore, some recent works have started to incorporate Self-Attention (SA) [23]–[25] into CNN architectures for diagnosis to add global attention rather than just local attention. Particularly, Wang et al. [25] propose a multi-level fundus image classification model MBSaNet that combines CNN and Self-Attention mechanisms. The convolutional block extracts local information of the fundus image, and the SA module further captures the complex relationship between different spatial positions, thereby directly detecting one or more fundus diseases in the fundus image. Experimental results show that MBSaNet achieves state-of-the-art performance with fewer parameters on two different datasets. These works demonstrate that the attention mechanism is promising in disease classification diagnosis.

B. Transformer based Methods

Due to the excellent performance of the vanilla Transformer in various computer vision tasks, many recent works [12], [26]–[29] have explored the effectiveness of the Transformer architecture to address the limitation of CNNs in fundus image classification. Especially, N. S. Kumar et al. [30] evaluate the DR grading architectures of Transformer, CNN, and Multi-Layer Perceptron (MLP) in terms of model convergence time, accuracy, and model scale, demonstrating that the Transformer-based model outperforms the CNN and MLP architectures in terms of not only accuracy but also achieving comparable model convergence time.

Currently, methods based on the Transformer backbone for retinal disease diagnosis can be roughly divided into two types: using only the Transformer and combining the Transformer with CNN for extracting features. For the former, notably, Yu et al. [12] first use ViT for retinal disease classification tasks by pre-training the Transformer model for downstream retinal disease classification tasks. In addition, to fully utilize the feature representation extracted from a single image patch, they propose a MIL head based on multi-instance learning (MIL). They test on DR grading dataset APTOS2019 and dataset RFMiD2020, respectively, and achieve state-of-the-art performance. Similarly, Jiang et al. [26] also verify the effectiveness of the ViT backbone for classifying retinal

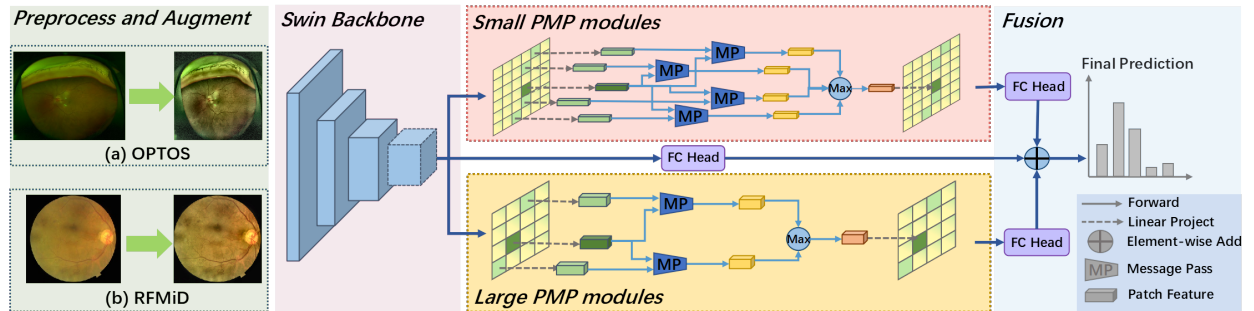


Fig. 1. The framework of our proposed method. Firstly, the retinal images undergo preprocessing and data augmentation and are then fed into the Swin Transformer backbone to obtain a semantic feature map. This map is then linearly transformed and inputted into two branches, namely PMP modules for small patches and PMP modules for large patches, to obtain new feature maps. The three resulting semantic feature maps are fused and used to compute the final prediction.

disease. They design an innovative saliency enhancement module and abnormality-aware attention to distinguish the main abnormal regions as well as the small subtle lesions for better diagnosis. For the latter, Yang et al. [29] propose a method called TransEye which combines the advantages of CNN and ViT, enabling effective extraction of bottom-level features and establishing long-range dependencies in the images. Experimental evaluations conducted on the OIA-ODIR dataset demonstrated that the TransEye method achieves much higher optimal prediction accuracy compared to CNN and ViT. From the identified Transformer-related works, it can be observed that the Transformer has great potential to achieve excellent performance in retinal disease diagnosis tasks, surpassing most CNNs. The current challenge is how to innovate upon the Transformer-based architecture in order to make it more applicable for retinal disease diagnosis.

III. METHOD

A. Overview

The proposed method is illustrated in Fig. 1. After preprocessing and data augmentation, the input image is fed into the Swin V2 [31] backbone to obtain a feature map consisting of many patches. The semantic feature map is then directed into dual branches of PMP modules to establish global connections between semantic features of different lesion scales through patch message aggregation. The output results of the two branches and the main trunk classifier will be used separately to calculate the Cross-Entropy loss.

B. Preprocessing and Data Augmentation

Our proposed method has been evaluated using two distinct datasets.

1) *OPTOS Dataset*: The first dataset, OPTOS, comprises 1033 high-definition color fundus images captured using advanced ultra-widefield cameras manufactured by Optos. These images cover more than 80% or 200° of the retina in a single capture. The dataset is categorized by several experienced ophthalmologists into seven classes: DME, High Myopia, Hypertension, Uveitis, Retinal Vein Occlusion (RVO), Retinal Detachment, and Normal, which is shown in Table I. The images have varying resolutions ranging from 714×545 to

3900×3072 . To facilitate comparison with other methods, all images were resized to a standardized scale of 384×384 . We augment the datasets using various data augmentation techniques to mitigate the adverse effects of class imbalance on model performances. Specifically, we apply CLAHE, Gaussian blur, horizontal and vertical flips, affine transformations, and color jittering to achieve a balanced distribution.

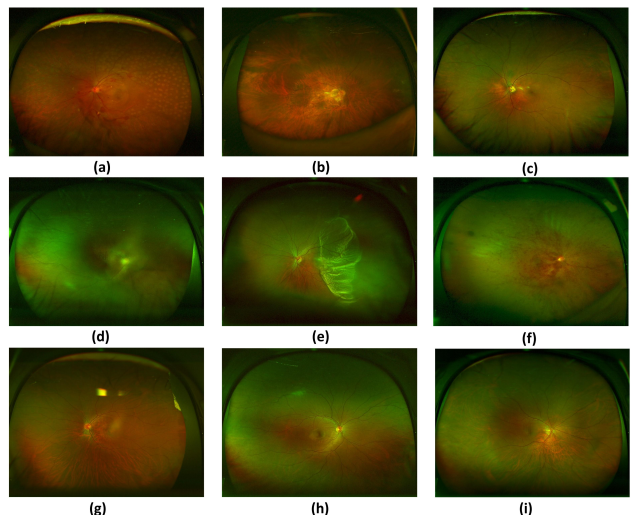


Fig. 2. Sample images in OPTOS dataset, a: DME, b: High Myopia, c: Hypertension, d: Uveitis, e: Retinal Detachment, f: RVO, g-i: Normal.

TABLE I
DISTRIBUTION OF OPTOS DATASET

Category	Unbalanced			Balanced		
	Train	Val	Test	Train	Val	Test
DME	49	12	16	160	40	50
High Myopia	156	40	49	160	40	50
Hypertension	64	16	20	160	40	50
RVO	133	34	42	160	40	50
Retinal Detachment	20	16	63	160	40	50
Uveitis	130	33	41	160	40	50
Normal	63	16	20	160	40	50
Total	615	167	251	1120	280	350
	1033			1750		

2) *RFMiD Dataset*: Additionally, we utilize an open-source multi-labeled Retinal Fundus Multi-Disease Image Dataset

(RFMiD) [32] for the second dataset. This dataset, collected from the Eye Clinic of Sushrusa Hospital in collaboration with the Centre of Excellence in Signal and Image Processing, SGGs Institute of Engineering and Technology, India, comprises 1920 color fundus images with 46 different categories. As RFMiD is a multi-labeled dataset, each fundus image may belong to more than one disease category. Due to the limited number of images in certain categories, which is insufficient for training deep learning models, single-label images with a count of at least 100 are selected from each category to ensure a balanced distribution of data following the previous method [21]. This results in the selection of four categories, namely DR, MH, ODC, and Normal, shown in Table II. Subsequently, we apply the same preprocessing and data augmentation techniques as employ our own dataset to balance the distribution in RFMiD. Fig. 1 displays the results of the preprocessing and data augmentation techniques.

TABLE II
DISTRIBUTION OF RFMID DATASET

Category	Unbalanced			Balanced		
	Train	Val	Test	Train	Val	Test
DME	163	41	36	306	76	68
MH	122	31	27	306	76	68
ODC	80	21	18	306	76	68
Normal	272	68	61	306	76	68
Total	637	168	142	1224	304	272
	947			1800		

C. Message Passing Module

When it comes to classification tasks, it is common practice to feed the entire feature map into a linear classifier to get the final logits. However, this method can result in the loss of semantic information on lesion regions in fundus images. To make the most of the feature representations of the feature map, we utilize patches and input them into our specially designed PMP modules to create semantic associations.

Initially, the input image $X \in R^{H \times W \times 3}$ is divided into a collection of non-overlapping patches with size 4×4 by patch partition, where $H, W, 3$ denotes the height, width and the number of channels, respectively. Then, these patches are fed into the Transformer blocks, generating the feature map with a dimension of $\frac{H}{32} \times \frac{W}{32} \times 8C$ [33], consisting of $\frac{H}{32} \times \frac{W}{32}$ patches with a dimension of $1 \times 1 \times 8C$.

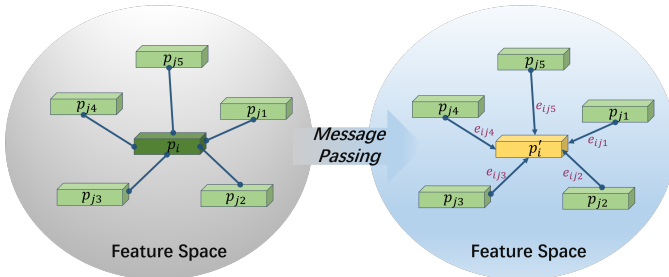


Fig. 3. Patch message passing. Each patch's feature is represented by p , and the connections between patches indicate their adjacency in feature space. The message transmitted between two patches is represented by e .

Algorithm 1: Multi-scale Patch Message Passing

Input: \mathcal{M} : Semantic feature map output by Swin backbone
 S_s : Size of small patch
 S_k : k nearest neighbor patches of small branch
 S_n : Number of small PMP modules
 L_s : Size of large patch
 L_k : k nearest neighbor patches of large branch
 L_n : Number of large PMP modules

Output: \mathcal{F} : Final prediction

- Regarding the primary branch, \mathcal{M} is transmitted through the fully connected layer, producing the logit value of y' :

$$y' = FC(\mathcal{M});$$
- For the branch of the large patch

$$P_L = LinearProject(\mathcal{M}, L_s) = \{p_1, p_2, \dots, p_{L_m}\};$$
for 1 to L_n do
 - for $p_i \leftarrow p_1$ to p_{L_m} do**
 - Propagate messages from the L_k nearest neighbors in the feature space

$$\{p_{j1}, p_{j2}, \dots, p_{jL_k}\} = KNearest(P_L, p_i);$$
 - $p_i = \max_{p_j \in \{p_{j1}, p_{j2}, \dots, p_{jL_k}\}} Message(p_i, p_j);$
 - end**
- end**

- Calculate the logit y'' output by the branch of the large patch

$$y'' = FC(P_L);$$
- For the branch of the small patch

$$P_S = LinearProject(\mathcal{M}, S_s) = \{p_1, p_2, \dots, p_{S_m}\};$$
for 1 to S_n do
- for $p_i \leftarrow p_1$ to p_{S_m} do**
 - Propagate messages from the S_k nearest neighbors in the feature space

$$\{p_{j1}, p_{j2}, \dots, p_{jS_k}\} = KNearest(P_S, p_i);$$
 - $p_i = \max_{p_j \in \{p_{j1}, p_{j2}, \dots, p_{jS_k}\}} Message(p_i, p_j);$
- end**
- end**
- Calculate the logit y''' output by the branch of the small patch

$$y''' = FC(P_S);$$
- $\mathcal{F} = Softmax(Mean(y', y'', y'''));$
- return** \mathcal{F}

Specifically, inspired by Message Passing Neural Networks (MPNNs) [34], [35], we adapt graph convolution operations to transmit and aggregate information between patches with similar features, which allows patches with receptive fields corresponding to the lesion regions to directly establish semantic relationships dynamically. Shown in Fig. 3, we consider each patch feature as a graph node p , and then the feature map with n patches can be represented as $P = \{p_1, \dots, p_n\} \subseteq R^{1 \times 1 \times F}$. F denotes the feature dimension of each patch. During the subsequent message passing, patches with similar semantic features are connected to build a graph using k -

nearest neighbors in the feature space, i.e., we construct the directed graph $G = (V, E)$, where vertices $V = \{1, 2, \dots, n\}$ and edges E are defined as:

$$E = \{e_{ij} \mid i, j \in \{1, 2, \dots, n\}, i \neq j\} \subseteq V \times V. \quad (1)$$

Here, e_{ij} represents the edge connecting p_i and p_j as a nonlinear mapping of the semantic information of the two patches, which is defined as:

$$e_{ij} = h_{\Theta}(p_i, p_j - p_i), \quad (2)$$

where h_{Θ} denotes a neural network with a set of learnable parameters Θ . It can be defined as:

$$h_{\Theta}(\cdot) = \text{Dropout}(\text{LeakyReLU}(\text{LayerNorm}(\text{Linear}(\cdot))))), \quad (3)$$

where *Linear* represents a linear layer responsible for transforming the input data into a new representation, *LayerNorm* represents a layer-normalization layer that helps to improve the stability and efficiency of the network, *LeakyReLU* is an activation function that introduces nonlinearity into the model, and *Dropout* represents a dropout layer that serves to mitigate the risk of overfitting by randomly dropping out specific units during training. After the message aggregation, each patch is updated to:

$$p'_i = \max_{j:e_{ij} \in E} e_{ij}, i \in \{1, 2, \dots, n\}. \quad (4)$$

We stack multiple PMP modules to enable dynamic interaction of pathological semantic features, thus effectively establishing global relationships.

D. Multi-Scale Patch

Due to the varied location and size of lesion areas in different retinal diseases, if the patch size is too small, it is likely to aggregate information from similar patches rather than neighboring patches, which can lead to a convolution-like operation and hinder the establishment of global connections. To fuse information from patches over long distances, it is necessary to perform multiple information aggregation operations on individual patches, which results in higher FLOPs and memory consumption. Conversely, if the patch size is too large, it is difficult to extract detailed image information. Therefore, our proposed approach aims to capitalize on the benefits of utilizing smaller patch sizes, while also ensuring that the overall complexity is properly balanced. Specifically, we have added two PMP module branches to the Transformer, targeting different patch sizes, as described in Algorithm 1. As for the large branch, we concatenate adjacent L_s patches in the feature dimension to represent a larger patch. Therefore, a total of $\frac{H}{32 \times L_s} \times \frac{W}{32 \times L_s}$ patches are inputted into the PMP modules of the large branch. Similarly, after the linear transform, a total of $\frac{H}{32 \times S_s} \times \frac{W}{32 \times S_s}$ patches are sent into corresponding PMP modules. Finally, we obtain three feature maps including \mathcal{M} , P_L , and P_S , which we feed into the FC head to obtain corresponding logits. We calculate the loss for each of the three logits separately using CE loss. Our loss function can be denoted as:

$$L(y, y', y'', y''') = -\frac{1}{3} \sum_{i=0}^C y_i \log(y'_i y''_i y'''_i), \quad (5)$$

where y represents the ground truth and C represents the number of categories. The primary branch, large branch, and small branch output logits are represented by y' , y'' , and y''' , respectively.

IV. EXPERIMENTAL SETUP AND RESULTS

A. Metrics

The Performance evaluation is based on four metrics, namely Accuracy, Precision, F1, and Cohen's Kappa, which are given by:

$$\text{Accuracy} = \frac{\text{True Positive} + \text{True Negative}}{\text{Positive} + \text{Negative}} \quad (6)$$

$$\text{Precision} = \frac{\text{True Positive}}{\text{True Positive} + \text{False Postive}} \quad (7)$$

$$\text{Recall} = \frac{\text{True Positive}}{\text{True Positive} + \text{False Negative}} \quad (8)$$

$$F1 = 2 * \frac{\text{Precision} * \text{Recall}}{\text{Precision} + \text{Recall}} \quad (9)$$

$$\text{Kappa} = \frac{P_o - P_e}{1 - P_e} \quad (10)$$

$$P_o = \frac{\text{True Positive} + \text{True Negative}}{\text{Positive} + \text{Negative}} = \text{Accuracy} \quad (11)$$

$$P_e = \frac{\sum_{i=1}^C (a_i \times b_i)}{N \times N}, \quad (12)$$

where a_i refers to the number of the practical samples for class i , b_i refers to the number of the predicted samples for class i , C is the number of classes and N is the number of total samples.

B. Implementation Details

Using Python based on the PyTorch platform [39], all methods are implemented on 4 Nvidia GeForce RTX 3090Ti GPUs, each with 24GB memory. The input images are first resized to a standard size of 384×384 and then undergo random augmentation using Python's Albumentations library [40]. The optimizer utilized is Adam, with the learning rate updated using cosine annealing. All model backbones are initialized with pre-trained ImageNet [41] weights to enhance performance and speed up convergence. The division of the training and testing sets is shown in Table I and II, with the proportion of OPTOS and the public dataset being 0.8:0.2 and 0.85:0.15, respectively. To comprehensively evaluate the performance, we employ a five-fold cross-validation method and calculate the average results of the five models on the testing set. For all methods, we standardize the training process by conducting 150 epochs with a batch size of 8.

TABLE III
COMPARISON OF RESULTS OBTAINED BY DIFFERENT METHODS ON OPTOS DATASET

Category	Method	Unbalanced				Balanced			
		Accuracy(%)	Precision(%)	F1(%)	Kappa(%)	Accuracy(%)	Precision(%)	F1(%)	Kappa(%)
CNN	ResNet18 [19]	72.44 ± 2.16	72.32 ± 0.31	70.74 ± 1.01	67.19 ± 2.22	87.60 ± 1.66	88.02 ± 1.71	87.59 ± 1.72	85.53 ± 2.26
	ResNet50 [19]	71.95 ± 1.01	71.36 ± 1.29	70.61 ± 1.68	66.61 ± 1.47	89.49 ± 1.53	89.64 ± 1.36	89.48 ± 1.56	87.73 ± 2.08
	SE-ResNet [36]	76.25 ± 3.99	73.61 ± 9.13	73.62 ± 6.72	71.61 ± 5.12	90.00 ± 0.94	90.42 ± 0.68	89.90 ± 0.84	88.33 ± 1.27
	MobileNet [37]	74.90 ± 2.70	73.25 ± 1.52	72.29 ± 2.66	70.00 ± 3.44	88.97 ± 3.37	89.50 ± 3.46	89.07 ± 3.59	87.13 ± 4.59
Transformer	ViT [11]	74.81 ± 3.53	74.36 ± 3.84	72.32 ± 3.18	69.81 ± 4.30	89.26 ± 1.08	89.64 ± 1.01	89.33 ± 1.13	87.47 ± 1.48
	Cross-ViT [38]	74.57 ± 7.42	74.83 ± 7.16	72.36 ± 10.67	68.95 ± 6.82	88.46 ± 2.19	88.26 ± 4.23	88.48 ± 2.12	86.96 ± 2.96
	MIL-VT [12]	75.45 ± 6.40	74.06 ± 9.76	75.37 ± 8.76	73.19 ± 6.97	88.40 ± 1.08	88.67 ± 1.51	88.41 ± 1.38	86.47 ± 1.48
	Swin [31]	77.59 ± 2.38	75.20 ± 1.95	75.37 ± 2.60	73.19 ± 3.45	90.51 ± 3.19	90.76 ± 2.30	90.53 ± 2.96	88.93 ± 4.36
	PMP-Swin(Ours)	80.29 ± 1.04	78.60 ± 0.75	78.00 ± 0.79	76.36 ± 1.38	92.12 ± 0.27	92.29 ± 0.36	92.13 ± 0.29	90.80 ± 0.37

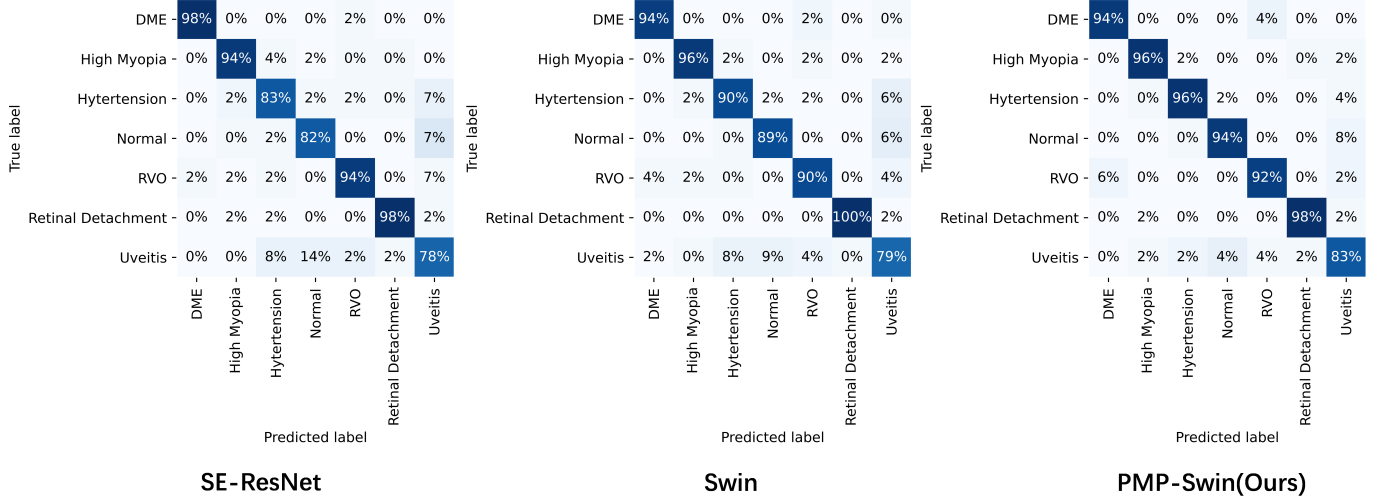


Fig. 4. Comparison of confusion matrices obtained from different methods on OPTOS dataset. The column and row denote the predicted and true labels, respectively. The intensity of the matrix entries is proportional to the magnitude of the corresponding values, with darker shades indicating higher values.

TABLE IV
COMPARISON OF RESULTS OBTAINED BY DIFFERENT METHODS ON BALANCED RFMiD DATASET

Category	Method	Accuracy(%)	Precision(%)	F1(%)	Kappa(%)
CNN	ResNet18 [19]	96.40 ± 0.40	96.45 ± 0.40	96.40 ± 0.42	95.20 ± 0.72
	ResNet50 [19]	95.15 ± 1.76	95.26 ± 1.62	95.13 ± 1.77	93.53 ± 3.12
	SE-ResNet [36]	96.40 ± 0.91	96.46 ± 0.85	96.40 ± 0.90	95.20 ± 1.61
	MobileNet [37]	95.37 ± 0.44	95.45 ± 0.37	95.36 ± 0.44	93.83 ± 0.79
Transformer	ViT [11]	95.96 ± 0.95	96.01 ± 0.89	95.96 ± 0.95	94.61 ± 1.68
	Cross-ViT [38]	95.37 ± 0.51	95.03 ± 2.60	95.40 ± 0.43	94.22 ± 0.05
	MIL-VT [12]	97.06 ± 0.61	97.10 ± 0.60	97.07 ± 0.62	96.08 ± 1.08
	Swin [31]	96.47 ± 1.12	96.53 ± 1.12	96.47 ± 1.12	95.29 ± 2.00
	PMP-Swin(Ours)	97.79 ± 0.47	97.83 ± 0.46	97.80 ± 0.46	97.06 ± 0.84

C. Experimental Results

In order to compare with previous methods, we conducted relevant work. Most latest methods for fundus disease classification are difficult to re-implement because of the lack of publicly available code, experimental details, or certain datasets [42]. Therefore, in addition to the methods specifically designed for fundus image classification, such as MIL-VT [12], we also select models commonly used as fundus disease classification benchmarks, such as ResNet18 and ResNet50 [19]. We divide them into CNN and Transformer methods based on their backbones.

As shown in Table III, our method achieve the best results in all four metrics on both the imbalanced dataset before resampling and the balanced dataset after resampling. Specifically,

regarding the Accuracy score, our method reaches 80.29% on the unbalanced OPTOS dataset, 2.7% higher than Swin and 4.04% higher than SE-ResNet [36], which shows its ability to better capture the complex and subtle patterns in fundus images. To further strengthen our argument, we also test our method on the publicly available RFMiD dataset. Table IV shows that our method also achieves the highest scores in all metrics on balanced RFMiD.

To further analyze the classification results, we present confusion matrix results as shown in Fig. 4. Due to the similarity of features between Uveitis disease, Hypertension, and Normal on fundus images, it presents a challenge for models to classify these three types of diseases accurately. However, our approach outperforms SE-ResNet and Swin in the category of the three diseases. The result indicates our

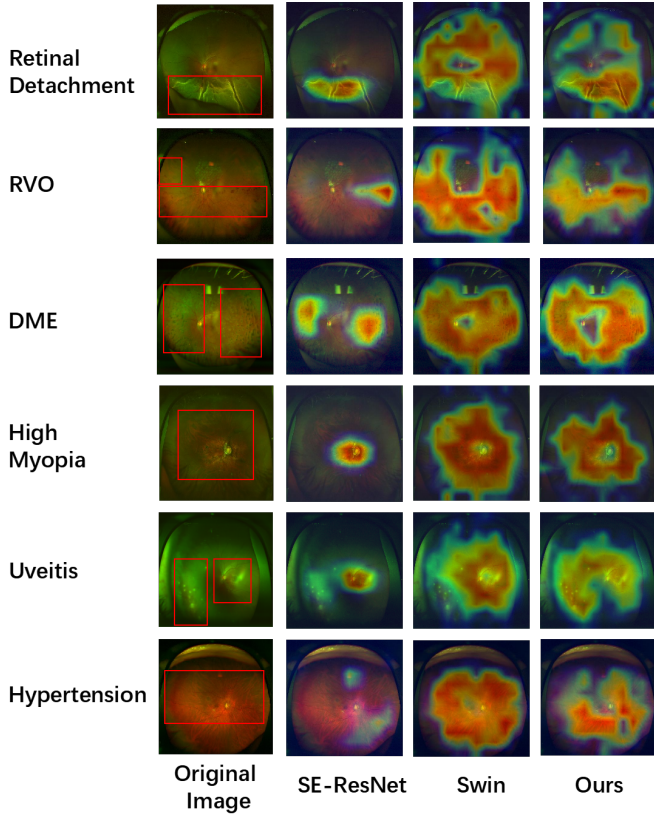


Fig. 5. Comparison of Grad-CAM heatmaps of each class obtained by different methods on OPTOS dataset. Lesion location is indicated by the red box.

method can capture fine-grained features better.

In addition to the aforementioned quantitative result comparisons, we also use the Grad-CAM [43] method to visualize the model performance. The color gradient indicates the degree of pixel attention in the heatmap generated by Pytorch Grad-CAM library [44], where deeper shades of red indicate greater attention and deeper shades of blue indicate weaker attention. It can be seen in Fig. 5 and Fig. 6 that the focused area of SE-ResNet based on CNN structure is relatively concentrated due to its local receptive field. However, the focused areas of Swin and our method based on Transformer structure are dispersed due to their global receptive field, which can focus on more lesion areas. Compared to Swin, our method can more accurately focus on most lesion areas rather than the normal retinal background. In addition, as shown in Fig. 6 for the DR class, our model can accurately identify hard exudates, as demonstrated by both the global heatmap and local heatmaps.

D. Ablation Studies

This section presents our ablation study on the OPTOS dataset. Firstly, we validate the effectiveness of the PMP module and then analyze the robustness of our method with different parameters in our architecture design, including patch size, number of PMP modules, and the K value required for information aggregation.

1) *The effectiveness of Multi-Scale Patch Message Passing Module:* Table V demonstrates that the introduction of the

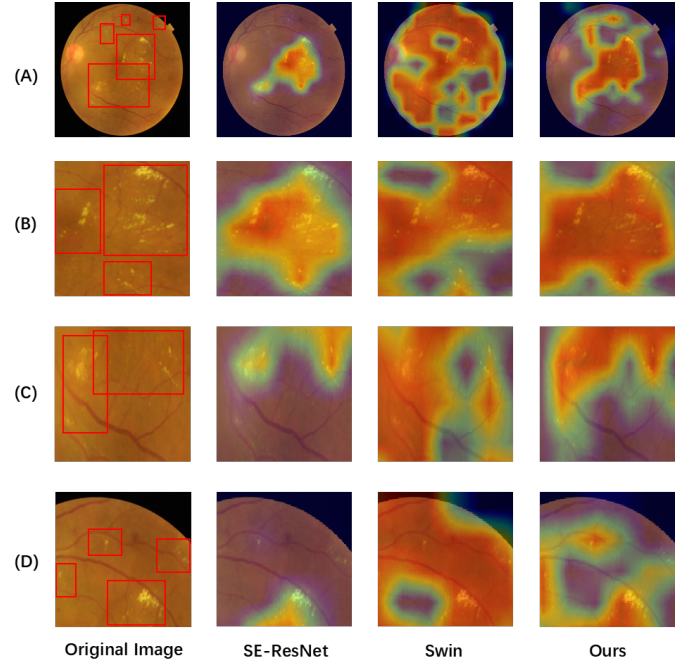


Fig. 6. Comparison of Grad-CAM heatmaps of DR class obtained by different methods on RFMiD dataset. The lesion location is indicated by the red box. Row A displays the global view along with its corresponding heatmaps, while rows B, C and D represent local views and their respective heatmaps.

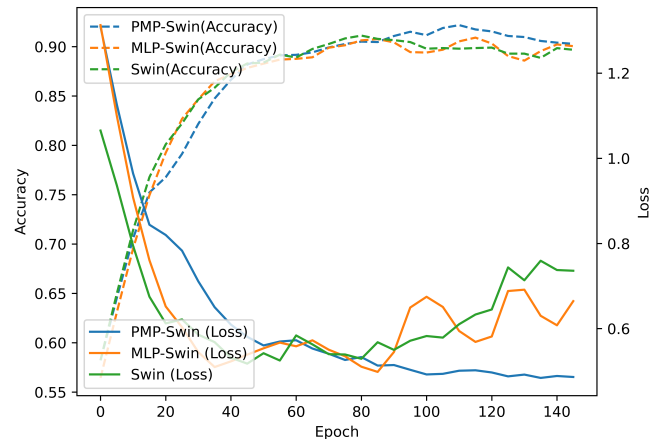


Fig. 7. Comparison of valid accuracy and train loss curves obtained by methods based on Swin backbone on OPTOS dataset.

PMP module can effectively improve the performance of the Swin backbone. To be more specific, the Accuracy score of PMP-Swin increases by 2.7% on the unbalanced OPTOS dataset and 1.61% on the balanced OPTOS dataset. However, replacing PMP modules with MLP layers results in decreased performance compared with Swin, especially on the unbalanced OPTOS dataset, with the Accuracy score decreasing by 2.11%. It may be because constructing more complex feature representations of semantic features with simple linear layers cannot exploit useful information for better classification.

To verify the necessity of multi-scale branches, we compare

TABLE V
COMPARISON OF RESULTS OBTAINED BY DIFFERENT COMBINATION METHODS BASED ON SWIN STRUCTURE ON OPTOS DATASET

Method	Combination			Unbalanced				Balanced			
	MLP	PMP	Multi-Scale	Accuracy(%)	Precision(%)	F1(%)	Kappa(%)	Accuracy(%)	Precision(%)	F1(%)	Kappa(%)
Swin				77.59 ± 2.38	75.20 ± 1.95	75.37 ± 2.60	73.19 ± 3.45	90.51 ± 3.19	90.76 ± 2.30	90.53 ± 2.96	88.93 ± 4.36
MLP-Swin	✓			75.48 ± 4.03	74.51 ± 6.23	73.16 ± 4.50	70.66 ± 5.42	90.34 ± 0.92	90.50 ± 0.75	90.33 ± 0.87	88.73 ± 1.25
PMP(Mono)-Swin		✓		76.54 ± 3.19	75.04 ± 3.18	74.21 ± 1.90	71.91 ± 3.66	91.94 ± 0.30	92.39 ± 0.31	92.03 ± 0.29	90.60 ± 0.41
PMP-Swin(Ours)		✓	✓	80.29 ± 1.04	78.60 ± 0.75	78.00 ± 0.79	76.36 ± 1.38	92.12 ± 0.27	92.29 ± 0.36	92.13 ± 0.29	90.80 ± 0.37

the performance of PMP(Mono)-Swin with only one branch of PMP modules, and PMP-Swin with two branches of PMP modules. As shown in Table V, the classification performance of PMP-Swin is better than that of PMP(Mono)-Swin both before and after resampling, indicating that multi-scale branches can effectively improve classification performance. This may be due to that the diversity of lesion area sizes is taken into account when aggregating information in patches input to PMP modules, which is beneficial for establishing global connections of lesion features. Additionally, training of methods based on Swin backbone with different structures is given in Fig. 7. It can be observed that Swin and MLP-Swin overfit after training for 80 epochs, while our method’s loss curve continues to decrease until around 140 epochs, implying that our method can effectively prevent overfitting and achieve higher classification accuracy.

TABLE VI
COMPARISON OF RESULTS OBTAINED BY DIFFERENT STRUCTURE SETTINGS OF PMP-SWIN ON OPTOS DATASET

Method	Small Branch			Large Branch			Performance(%)
	Patch Size	K	N	Patch Size	K	N	
A	1	8	3	4	2	3	91.82 ± 0.72
B	2	8	3	4	2	3	91.50 ± 0.58
C	1	4	3	4	2	3	91.23 ± 0.50
D	1	8	2	4	2	3	91.22 ± 0.63
E	1	8	3	8	2	3	91.79 ± 0.55
F	1	8	3	4	2	2	91.25 ± 0.82
PMP-Swin(Ours)	1	8	3	4	4	3	91.84 ± 0.31

2) *Comparison of different structure settings:* Table VI shows the impact of different parameter settings on the average performance of our method across four metrics. With different settings, all models reach a high accuracy of over 91%, supporting our method’s effectiveness for robustness. Firstly, for patch size, we select different pairs of patch sizes including (1,4), (2,4), and (1,8), and the results showed that (1,4) achieved the best average performance. K represents how many most similar patches in the feature space each patch needs to select for information aggregation. Our experiments show that when the K of the small branch is 8 and the K of the large branch is 4, our method achieves the best performance. This issue may be attributed to the size of the patch. To be more specific, patch size determines the total number of patches. Secondly, when the patch size is too small, K should be appropriately increased, otherwise, it will lead to information aggregation only in local regions. When the patch size is too large, K should be reduced, otherwise, it will lead to information aggregation between patches containing semantic information and those containing too much non-lesion semantic information. In addition, we also consider the impact of the depth of both branches on the model. The best

performance is achieved when both branches have a depth of 3. It can be seen that when N is reduced, the model’s performance declines, indicating that a sufficient stack of PMP modules can extract more features.

E. CONCLUSION

In this paper, we present a novel framework named PMP-Swin for the classification of retinal diseases in fundus images, which incorporates two key improvements. Firstly, we introduce a new PMP module based on the Message Passing mechanism that can be easily integrated into the Transformer Backbone. This enables us to fully exploit patch features and establish global connections among disease-related features. Secondly, we utilize a dual-branch approach with PMP modules to learn features at multiple scales considering that the scale of pathological features varies among different diseases. Our extensive experiments on both private and public datasets demonstrate that our method outperforms current state-of-the-art techniques based on CNNs and Transformers. We believe that our proposed method can inspire more Transformer-based classification diagnostic techniques, which will further promote the application of deep learning in clinical diagnosis.

REFERENCES

- [1] Z. Fu, A. Usui-Ouchi, W. Allen, and Y. Tomita, “Retinal disease and metabolism,” *Reproductive and developmental Biology*, vol. 12, no. 2, p. 183, 2022.
- [2] G. Selvachandran, S. G. Quek, R. Paramesran, W. Ding, and L. H. Son, “Developments in the detection of diabetic retinopathy: a state-of-the-art review of computer-aided diagnosis and machine learning methods,” *Artificial intelligence review*, vol. 56, no. 2, pp. 915–964, 2023.
- [3] D. Chawla and A. Deorari, “Retinopathy of prematurity prevention, screening and treatment programmes: Progress in india,” in *Seminars in Perinatology*, vol. 43, no. 6. Elsevier, 2019, pp. 344–347.
- [4] L. Guo, J.-J. Yang, L. Peng, J. Li, and Q. Liang, “A computer-aided healthcare system for cataract classification and grading based on fundus image analysis,” *Computers in Industry*, vol. 69, pp. 72–80, 2015.
- [5] N. Saleh, M. Abdel Wahed, and A. M. Salaheldin, “Computer-aided diagnosis system for retinal disorder classification using optical coherence tomography images,” *Biomedical Engineering/Biomedizinische Technik*, vol. 67, no. 4, pp. 283–294, 2022.
- [6] A. Bourouis, M. Feham, M. A. Hossain, and L. Zhang, “An intelligent mobile based decision support system for retinal disease diagnosis,” *Decision Support Systems*, vol. 59, pp. 341–350, 2014.
- [7] S. C. Lee, E. T. Lee, R. M. Kingsley, Y. Wang, D. Russell, R. Klein, and A. Warn, “Comparison of diagnosis of early retinal lesions of diabetic retinopathy between a computer system and human experts,” *Archives of Ophthalmology*, vol. 119, no. 4, pp. 509–515, 2001.
- [8] S. Asif and K. Amjad, “Deep residual network for diagnosis of retinal diseases using optical coherence tomography images,” *Interdisciplinary Sciences: Computational Life Sciences*, vol. 14, no. 4, pp. 906–916, 2022.
- [9] Y.-t. Oh and H. Park, “End-to-end two-branch classifier for retinal imaging analysis,” in *2022 International Conference on Electronics, Information, and Communication (ICEIC)*. IEEE, 2022, pp. 1–3.

- [10] Y. Pan, J. Liu, Y. Cai, X. Yang, Z. Zhang, H. Long, K. Zhao, X. Yu, C. Zeng, J. Duan *et al.*, “Fundus image classification using inception v3 and resnet-50 for the early diagnostics of fundus diseases,” *Frontiers in Physiology*, vol. 14, p. 160, 2023.
- [11] A. Dosovitskiy, L. Beyer, A. Kolesnikov, D. Weissenborn, X. Zhai, T. Unterthiner, M. Dehghani, M. Minderer, G. Heigold, S. Gelly *et al.*, “An image is worth 16x16 words: Transformers for image recognition at scale,” *arXiv preprint arXiv:2010.11929*, 2020.
- [12] S. Yu, K. Ma, Q. Bi, C. Bian, M. Ning, N. He, Y. Li, H. Liu, and Y. Zheng, “Mil-vt: Multiple instance learning enhanced vision transformer for fundus image classification,” in *Medical Image Computing and Computer Assisted Intervention—MICCAI 2021: 24th International Conference, Strasbourg, France, September 27–October 1, 2021, Proceedings, Part VIII 24*. Springer, 2021, pp. 45–54.
- [13] J. Shen, Y. Hu, X. Zhang, Y. Gong, R. Kawasaki, and J. Liu, “Structure-oriented transformer for retinal diseases grading from oct images,” *Computers in Biology and Medicine*, vol. 152, p. 106445, 2023.
- [14] K. S. Lee, S. Lin, D. A. Copland, A. D. Dick, A. D. Dick, and J. Liu, “Cellular senescence in the aging retina and developments of neurotherapies for age-related macular degeneration.” *Journal of Neuroinflammation*, 2021.
- [15] L.-P. Cen, J. Ji, J.-W. Lin, S.-T. Ju, H.-J. Lin, T.-P. Li, Y. Wang, J.-F. Yang, Y.-F. Liu, S. Tan *et al.*, “Automatic detection of 39 fundus diseases and conditions in retinal photographs using deep neural networks,” *Nature communications*, vol. 12, no. 1, p. 4828, 2021.
- [16] V. Das, S. Dandapat, and P. K. Bora, “Automated classification of retinal oct images using a deep multi-scale fusion cnn,” *IEEE Sensors Journal*, vol. 21, no. 20, pp. 23 256–23 265, 2021.
- [17] N. Rajagopalan, V. Narasimhan, S. Kunnavakkam Vinjimoor, and J. Aiyer, “Deep cnn framework for retinal disease diagnosis using optical coherence tomography images,” *Journal of Ambient Intelligence and Humanized Computing*, vol. 12, pp. 7569–7580, 2021.
- [18] A. Sunija, S. Kar, S. Gayathri, V. P. Gopi, and P. Palanisamy, “Octnet: A lightweight cnn for retinal disease classification from optical coherence tomography images,” *Computer methods and programs in biomedicine*, vol. 200, p. 105877, 2021.
- [19] K. He, X. Zhang, S. Ren, and J. Sun, “Deep residual learning for image recognition,” in *Proceedings of the IEEE conference on computer vision and pattern recognition*, 2016, pp. 770–778.
- [20] F. Chollet, “Xception: Deep learning with depthwise separable convolutions,” in *Proceedings of the IEEE Conference on Computer Vision and Pattern Recognition (CVPR)*, July 2017.
- [21] N. Sengar, R. C. Joshi, M. K. Dutta, and R. Burget, “Eyedee-net: A multi-class diagnosis of retinal diseases using deep neural network,” *Neural Computing and Applications*, pp. 1–21, 2023.
- [22] X.-l. Yang and S.-l. Yi, “Multi-classification of fundus diseases based on dsra-cnn,” *Biomedical Signal Processing and Control*, vol. 77, p. 103763, 2022.
- [23] S. S. Mishra, B. Mandal, and N. B. Puhana, “Multi-level dual-attention based cnn for macular optical coherence tomography classification,” *IEEE Signal Processing Letters*, vol. 26, no. 12, pp. 1793–1797, 2019.
- [24] D. Das and D. R. Nayak, “Gs-net: Global self-attention guided cnn for multi-stage glaucoma classification,” in *2023 IEEE International Conference on Image Processing (ICIP)*, 2023, pp. 3454–3458.
- [25] K. Wang, C. Xu, G. Li, Y. Zhang, Y. Zheng, and C. Sun, “Combining convolutional neural networks and self-attention for fundus diseases identification,” *Scientific Reports*, vol. 13, no. 1, p. 76, 2023.
- [26] Y. Jiang, K. Xu, X. Wang, Y. Li, H. Cui, Y. Tao, and H. Lin, “Satformer: Saliency-guided abnormality-aware transformer for retinal disease classification in fundus image,” in *Proceedings of the Thirty-First International Joint Conference on Artificial Intelligence, IJCAI, 2022*, pp. 987–994.
- [27] Z. Ma, Q. Xie, P. Xie, F. Fan, X. Gao, and J. Zhu, “Hctnet: A hybrid convnet-transformer network for retinal optical coherence tomography image classification,” *Biosensors*, vol. 12, no. 7, p. 542, 2022.
- [28] C. Playout, R. Duval, M. C. Boucher, and F. Chérier, “Focused attention in transformers for interpretable classification of retinal images,” *Medical Image Analysis*, vol. 82, p. 102608, 2022.
- [29] H. Yang, J. Chen, and M. Xu, “Fundus disease image classification based on improved transformer,” in *2021 International Conference on Neuromorphic Computing (ICNC)*. IEEE, 2021, pp. 207–214.
- [30] N. S. Kumar and B. R. Karthikeyan, “Diabetic retinopathy detection using cnn, transformer and mlp based architectures,” in *2021 International Symposium on Intelligent Signal Processing and Communication Systems (ISPACS)*. IEEE, 2021, pp. 1–2.
- [31] Z. Liu, H. Hu, Y. Lin, Z. Yao, Z. Xie, Y. Wei, J. Ning, Y. Cao, Z. Zhang, L. Dong *et al.*, “Swin transformer v2: Scaling up capacity and resolution,” in *Proceedings of the IEEE/CVF conference on computer vision and pattern recognition*, 2022, pp. 12 009–12 019.
- [32] S. Pachade, P. Porwal, D. Thulkar, M. Kokare, G. Deshmukh, V. Sahasrabudhe, L. Giancardo, G. Quéllec, and F. Mériaudeau, “Retinal fundus multi-disease image dataset (rfmid): A dataset for multi-disease detection research,” *Data*, vol. 6, no. 2, p. 14, 2021.
- [33] Z. Liu, Y. Lin, Y. Cao, H. Hu, Y. Wei, Z. Zhang, S. Lin, and B. Guo, “Swin transformer: Hierarchical vision transformer using shifted windows,” in *Proceedings of the IEEE/CVF international conference on computer vision*, 2021, pp. 10 012–10 022.
- [34] J. Gilmer, S. S. Schoenholz, P. F. Riley, O. Vinyals, and G. E. Dahl, “Neural message passing for quantum chemistry,” in *International conference on machine learning*. PMLR, 2017, pp. 1263–1272.
- [35] Y. Wang, Y. Sun, Z. Liu, S. E. Sarma, M. M. Bronstein, and J. M. Solomon, “Dynamic graph cnn for learning on point clouds,” *ACM Transactions on Graphics (tog)*, vol. 38, no. 5, pp. 1–12, 2019.
- [36] J. Hu, L. Shen, and G. Sun, “Squeeze-and-excitation networks,” in *Proceedings of the IEEE conference on computer vision and pattern recognition*, 2018, pp. 7132–7141.
- [37] A. Howard, M. Sandler, G. Chu, L. Chen, B. Chen, M. Tan, W. Wang, Y. Zhu, R. Pang, V. Vasudevan, Q. V. Le, and H. Adam, “Searching for mobilenetv3,” *CoRR*, vol. abs/1905.02244, 2019. [Online]. Available: <http://arxiv.org/abs/1905.02244>
- [38] C.-F. R. Chen, Q. Fan, and R. Panda, “Crossvit: Cross-attention multi-scale vision transformer for image classification,” in *Proceedings of the IEEE/CVF international conference on computer vision*, 2021, pp. 357–366.
- [39] A. Paszke, S. Gross, F. Massa, A. Lerer, J. Bradbury, G. Chanan, T. Killeen, Z. Lin, N. Gimelshein, L. Antiga, A. Desmaison, A. Kopf, E. Yang, Z. DeVito, M. Raison, A. Tejani, S. Chilamkurthy, B. Steiner, L. Fang, J. Bai, and S. Chintala, “Pytorch: An imperative style, high-performance deep learning library,” in *Advances in Neural Information Processing Systems*, H. Wallach, H. Larochelle, A. Beygelzimer, F. d’Alché-Buc, E. Fox, and R. Garnett, Eds., vol. 32. Curran Associates, Inc., 2019.
- [40] A. Buslaev, V. I. Iglovikov, E. Khvedchenya, A. Parinov, M. Druzhinin, and A. A. Kalinin, “Albumentations: Fast and flexible image augmentations,” *Information*, vol. 11, no. 2, 2020. [Online]. Available: <https://www.mdpi.com/2078-2489/11/2/125>
- [41] J. Deng, W. Dong, R. Socher, L.-J. Li, K. Li, and L. Fei-Fei, “Imagenet: A large-scale hierarchical image database,” in *2009 IEEE conference on computer vision and pattern recognition*. Ieee, 2009, pp. 248–255.
- [42] M. A. Rodríguez, H. AlMarzouqi, and P. Liatsis, “Multi-label retinal disease classification using transformers,” *IEEE Journal of Biomedical and Health Informatics*, 2022.
- [43] B. Zhou, A. Khosla, A. Lapedriza, A. Oliva, and A. Torralba, “Learning deep features for discriminative localization,” in *Proceedings of the IEEE conference on computer vision and pattern recognition*, 2016, pp. 2921–2929.
- [44] J. Gildenblat and contributors, “Pytorch library for cam methods,” <https://github.com/jacobgil/pytorch-grad-cam>, 2021.